PHYSICAL REVIEW A **101**, 013408 (2020)

Doppler-cooled ions in a compact reconfigurable Penning trap

Brian J. McMahon,[*] Curtis Volin, Wade G. Rellergert, and Brian C. Sawyer
Georgia Tech Research Institute, Atlanta, Georgia 30332, USA

(Received 4 September 2019; published 8 January 2020)

We report the design and experimental demonstration of a compact, reconfigurable Penning ion trap constructed with rare-earth permanent magnets placed outside of a trap vacuum enclosure. We describe the observation of Doppler laser cooling of ions in a permanent magnet Penning trap. We detail a method for quantifying and optimizing the trap magnetic-field uniformity *in situ* using a thermal beam of neutral ^{40}Ca precursor atoms. Doppler laser cooling of ^{40}Ca$^+$ is carried out at 0.65 T, and side-view images of trapped ion fluorescence show crystalline order for both two- and three-dimensional arrays. Measured ^{40}Ca$^+$ trap frequencies confirm the magnetic-field characterization with neutral ^{40}Ca. The compact trap described here enables a variety of cold ion experiments with low size, weight, power, and cost requirements relative to traditional electromagnet-based Penning traps.

DOI: 10.1103/PhysRevA.101.013408

I. INTRODUCTION

Penning traps confine ions in three dimensions with a combination of a uniform magnetic field and quadrupolar electrostatic field. Unlike in radio-frequency (rf) Paul traps, ions in Penning traps exhibit no driven micromotion and, with the use of superconducting or permanent magnets, are confined with minimal power consumption. Traditional Penning traps consist of stacked hyperbolic or cylindrical electrode structures placed within the bore of a high-field ($\gtrsim$1 T) electromagnet operating with normal or superconducting currents. Such traps have enabled record-setting precision measurements of charged-particle masses [1] and magnetic moments [2–4]. Doppler laser cooling of ions in Penning traps was first demonstrated in the late 1970s [5], and has facilitated frequency metrology with hyperfine transitions exhibiting >550 s of coherent evolution [6] as well as precision measurements of hyperfine constants [7]. Recent work with laser-cooled ions in traditional Penning traps includes implementation of sub-Doppler laser cooling [8–10], sympathetic cooling of cotrapped molecular ions [11] and antimatter [12], spin entanglement verified by spin squeezing [13], quantum simulation of Ising magnetism [14,15], and optical force [16] (ion displacement [17]) detection with yN (pm) sensitivity.

Miniaturization of Penning traps using permanent magnets is attractive for reduction of required laboratory infrastructure (e.g., volume, cryogens, and power) and development of portable Penning traps. Replacement of large (>1 m^3) electromagnets with smaller ($\approx 10^{-4}$ m^3) rare-earth permanent magnets (REPMs) confers, for example, improved optical access for ion interrogation and imaging, shorter overall laser beam paths, and reduced fringing magnetic fields. Over the past three decades, a number of compact Penning traps based on REPMs have been demonstrated for applications including portable mass spectrometry [18], ion storage [19–21], and spectroscopy of highly charged ions [22]. Rare-earth magnets of the SmCo and NdFeB varieties have remanences and coercivities >1 T, allowing for Penning confinement of ions with masses up to ≈100 amu with a trap size, weight, power consumption, and cost each more than an order of magnitude below those of traditional high-field electromagnets. Notably, REPM materials have also been used in conjunction with rf Paul traps in the application of large magnetic gradients [23] and stable bias magnetic fields [24]. For precision measurements and quantum control experiments in Penning traps,

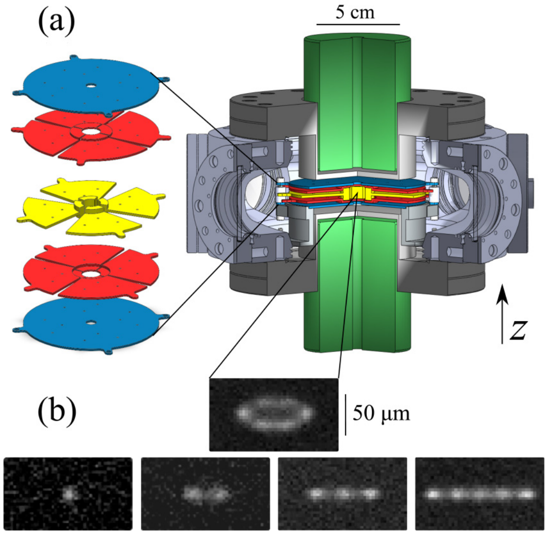

FIG. 1. (a) Left: Axially expanded trap electrode structure showing endcap (blue), compensation (red), and ring electrodes (yellow). Right: Section view of assembled trap. The NdFeB cylindrical ring magnets (green) are shown at the optimal spacing for maximum field uniformity. (b) Side-view images of Doppler-cooled samples of 1–20 ^{40}Ca$^+$ ions in three-dimensional (upper image) and two-dimensional (bottom row) configurations.

---

[*] brian.mcmahon@gtri.gatech.edu

maximizing magnetic-field uniformity and stability is critical to minimizing systematic errors due to fluctuating trap and internal atomic transition frequencies [25].

In this paper, we report the Doppler laser cooling of ions (^{40}Ca^{+}) in a compact Penning trap made with REPMs. In contrast to previous work, the trap magnets reside outside the vacuum vessel, making the trap magnetic field quickly reconfigurable. This feature also permits installation of REPMs with the highest remanence (N52 grade NdFeB, ≈60 °C working temperature) *after* the high-temperature vacuum bake. The trap operates at room temperature and ultrahigh vacuum ($<10^{-10}$ Torr), and ^{40}Ca^{+} samples can be trapped and cooled for days with no observed ion loss. We also document a procedure for optical characterization of the Penning trap magnetic environment using neutral precursor (^{40}Ca) atoms, substantially simplifying optimization of the REPM placement before trapping ions. This optical magnetic-field characterization is applicable to a wide range of Doppler-cooled atomic ion species in both REPM- and electromagnet-based Penning traps.

II. PENNING TRAP DESIGN AND CHARACTERIZATION

Figure 1(a) shows a drawing of the compact Penning trap used for this paper. The trap electrodes are constructed as a five-layer stack of Ti plates machined to a tolerance of ≈127 μm [left image of Fig. 1(a)], each referenced above and below via sapphire beads and washers (not shown). On the top and bottom are two endcap electrodes (blue) with 6-mm-diameter central holes for future axial laser beam access. Two sets of quarter-segmented harmonic compensation electrodes (red) allow for minimization of trap-potential anharmonicity and correction of misalignment between the electrode axis and trap magnetic field [26]. In the center of the electrode stack is the quarter-segmented ring electrode (yellow). In addition to contributing to the dc trap potential, the segmented electrodes permit application of a rf axialization drive [27] or a multipole rotating wall potential [28]. Side-view imaging and laser beam access are facilitated via the four 2 × 6-mm gaps in the segmented ring electrode. The trap geometry affords a maximal radial beam angle of $\approx \pm 5.5^{\circ}$.

A pair of commercial NdFeB (specified grade N52) cylindrical ring magnets with axial magnetization [green cylinders in Fig. 1(a)] provides the vertical Penning trap magnetic field. The sintered REPMs are fixed in Al tube clamps (not shown) for position adjustments relative to the 316LN stainless steel vacuum chamber. For cylindrical magnets, there exists a point along the axis where the second-order magnetic-field curvature vanishes (see the Appendix and Ref. [29]). Additionally, with identical axially separated magnets we remove all odd-order field curvature at the trap center.

Each magnet used for this trap has a 6.35-cm (2.5 in.) outer diameter, has a 0.79-cm (5/16 in.) inner diameter, and is 7.62 cm (3 in.) long. With this magnet geometry, we predict an optimal vertical spacing of 30 mm, a residual *quartic* vertical (radial) field curvature of -43 mG/mm^{4} (-15 mG/mm^{4}), and a magnetic field of 7215 G at the trap center. For comparison, Biercuk *et al.* report a residual *quadratic* radial field curvature of 1.8 mG/mm^{2} in a conventional superconducting magnet at a nominal magnetic field of ≈4.5 T [30]. For ion crystals with radii below ≈350 μm, our REPM-based trap can exhibit superior absolute field uniformity across the ion sample, albeit with a fractional field variation five times larger than in the superconducting magnet of Ref. [30].

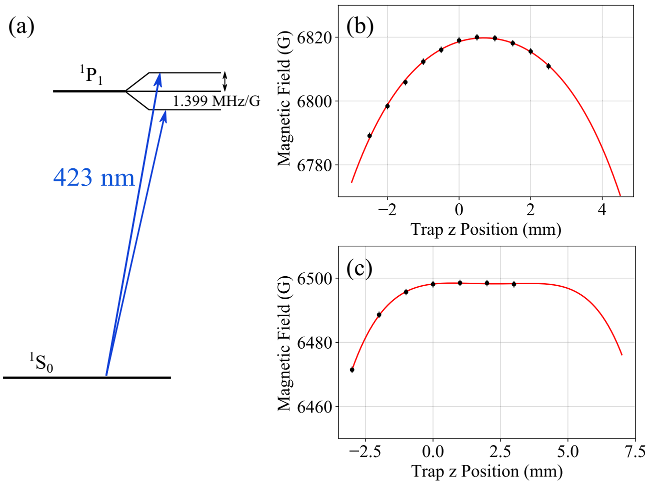

FIG. 2. Measurement of vertical (z) trap magnetic-field curvature using a thermal beam of ^{40}Ca precursor atoms. (a) Level diagram of ^{40}Ca showing the two transitions used for optical magnetometry. (b) Measure of the trap magnetic field as a function of axial position relative to the trap electrode center. Black points with error bars (standard error) are the measured data. For many data points, the error bars are smaller than the points. Red curves are fits to a multipole analytic model for cylindrical magnets [29]. The fit gives a magnet separation of 26.9(1) mm. (c) Same measurement as in (b) after increasing the magnet separation by 3 mm to the optimal spacing. The fit gives a final separation of 30.0(1) mm. Error bars show standard error that includes the frequency instability of the 423-nm laser.

The thermal sensitivity of NdFeB remanence is specified to be -0.12%/K near room temperature (i.e., -8.7 G/K at 7215 G), which provides a means of tuning the field magnitude. By placing the magnets outside the vacuum apparatus, we allow for realtime magnet adjustments and facilitate the use of NdFeB, which would otherwise be strongly demagnetized during our 190 °C vacuum chamber bakeout. Using a resistance temperature detector, we measure a magnet temperature instability of 20 mK over 1 h. At 1 s, the temperature fluctuations are below the 5-mK instrument resolution. For durations above 1 h, the measured magnet temperature instability matches that of the surrounding laboratory.

The trap magnetic-field curvature is mapped *in situ* in the vertical direction using the frequency-dependent fluorescence of neutral ^{40}Ca from an atomic oven. The atomic oven is constructed from Ta tubing and wire. The Ta tubing is filled with slivers of Ca, and the oven is mounted outside the Ti electrode structure directed radially toward the trap center. In a magnetic field, the $^{1}P_{1}$ state of ^{40}Ca is split into three levels—two magnetically sensitive levels ($m_J = \pm 1$) and one insensitive state ($m_J = 0$) [see Fig. 2(a)]. Here, m_J is the projection of electron angular momentum along the trap magnetic field. We scan a wavemeter-stabilized 423-nm laser through resonance at each of the two magnetically sensitive $^{1}S_{0} \rightarrow {}^{1}P_{1}$ transitions using an acousto-optic modulator

(AOM). The power-stabilized 423-nm laser beam is oriented perpendicular to the nominal atomic beam velocity to minimize the large Doppler shift from the ^{40}Ca forward velocity. The difference between the two measured optical frequencies is sensitive to the absolute magnetic field at the level of $\approx$2.799 MHz/G. To span the large ($\approx$20 GHz) frequency difference between atomic lines, we shift the wavemeter lock setpoint. The wavemeter lock provides laser frequency drift compensation with $\approx$2-Hz feedback bandwidth, and we measure a rms frequency instability below ± 1 MHz as confirmed with a scanning Fabry-Perot cavity [31]. We map the vertical (z) trap magnetic-field distribution by simultaneously translating the focused 423-nm beam and a fused silica imaging objective (NA $= 0.17$, $f/2.86$). The measurements are repeated at different positions within the 6-mm vertical electrode gap. Subtraction of the two optical transition frequencies at each vertical position removes the effects of frequency offsets due to slow drifts of atomic velocity or laser beam angle.

Figures 2(b) and 2(c) show the result of our magnetic-field measurements (black points with error bars) with fitted profiles (red lines). We fit to an analytic solution of the magnetic field due to axially magnetized cylinders derived in Ref. [29]. We vary and extract three experimental parameters from the fits: the magnet spacing, vertical center offset from the electrode center, and remanence of the magnet pair (see the Appendix). The fit of the data in Fig. 2(b) shows that the magnet pair center is initially 0.69(2) mm higher than our nominal trap electrode center, the magnetization is 13 309(14) G, and the magnet spacing is smaller than intended at 26.9(1) mm. After increasing the magnet spacing and repeating the axial field measurement, the fit to the data in Fig. 2(c) gives a spacing of 30.0(1) mm with an offset of 2.29(5) mm from the electrode center and a remanent magnetization of 13 395(13) G. The pull force between the magnets at this spacing is >500 N ($\approx$120 lb), and the magnets are strongly self-centering to a common axis. The most likely cause of the 0.6% discrepancy in the remanence between the two fits is a small overall offset (<1 mm) of the magnet axis from the trap electrode axis. The measured magnet remanences are closer to that of grade N45 than N52 NdFeB, and the ultimate measured uniform field value is 6498(1) G instead of the predicted 7215 G. This 10% lower magnetization could be the result of partial demagnetization during REPM handling or misidentification by the manufacturer.

III. TRAPPING AND DOPPLER COOLING ^{40}Ca^{+}

To create ^{40}Ca^{+} near the trap center and ensure precise overlap of the laser beams, all photoionization (PI) and Doppler-cooling laser beams are coaligned to the 423-nm beam. For ion creation at arbitrary magnetic field, the 423-nm laser is tuned to be resonant with the field insensitive $|^1S_0, m_J = 0\rangle \rightarrow |^1P_1, m_J = 0\rangle$ transition [see Fig. 2(a)]. A second photon with a wavelength below $\approx$390 nm is sufficient for Ca ionization [32]. We have loaded ^{40}Ca^{+} with $\approx$1 mW of CW 375- or 313-nm light as well as with a pulsed 266-nm source ($\approx$10 μJ, 30-ps pulse duration) produced from the fourth harmonic of a 1064-nm Nd:YAG laser. We vary the number of ions loaded by adjusting the power of the second PI laser beam [see Fig. 1(b)].

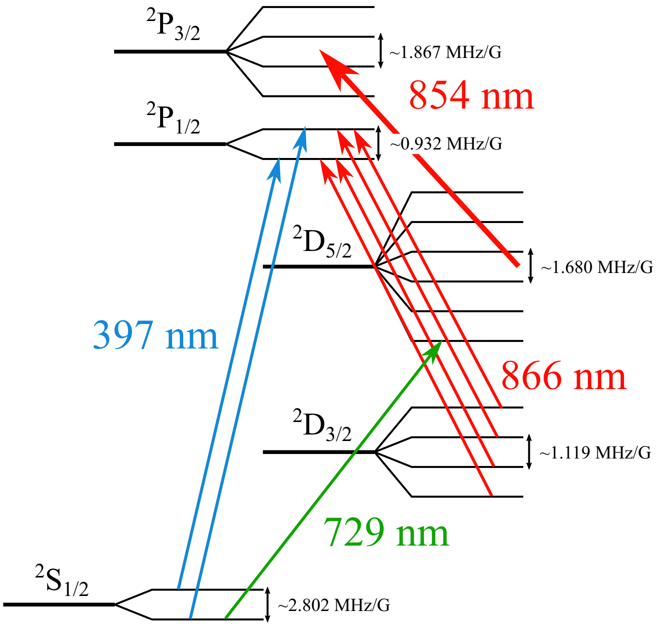

FIG. 3. Level diagram for ^{40}Ca^{+}, the optical transitions used in the experiment, and the magnetic sensitivity of each multiplet.

At the magnetic-field values used in this paper, the linear Zeeman effect splits the energy levels of ^{40}Ca^{+} by more than 10 GHz (see Fig. 3). For this reason, more laser frequencies are required to efficiently Doppler cool the trapped ion cloud than are needed at low field [33]. We use two separate external cavity diode lasers (ECDLs) near 397 nm to drive the $|S_{1/2}, m_J = \pm 1/2\rangle \rightarrow |P_{1/2}, m_J = \mp 1/2\rangle$ transitions. One also needs four repump frequencies near 866 nm to empty the long-lived $D_{3/2}$ level. Those frequencies are generated by tuning a single 866-nm ECDL to the unshifted repump frequency and coupling it through a broadband fiber electro-optic modulator (EOM). Two different modulation frequencies are applied to the EOM, creating the four sideband laser tones needed for repumping out of the $D_{3/2}$ states. Further complicating the cooling process, large external magnetic fields couple like-m_J states across fine-structure doublets (e.g., $P_{1/2}$ and $P_{3/2}$, $D_{3/2}$ and $D_{5/2}$), allowing spontaneous emission along the otherwise forbidden $P_{1/2} \rightarrow D_{5/2}$ pathway [34]. Because the large field only couples the like-m_J states, $m_J = \pm 5/2$ remain unpopulated. We apply an 854-nm laser beam to repump ions from the $D_{5/2}$ level back into the cooling cycle, and in practice we observe the same ion fluorescence whether or not sidebands are applied to the 854-nm light. We measure a $\approx$50% reduction in ^{40}Ca^{+} fluorescence with the 854-nm laser beam blocked, which suggests that our observed rate for $P_{1/2} \rightarrow D_{5/2}$ decays is similar to the $D_{5/2}$ spontaneous decay rate of $\approx$1.2 s^{-1}.

Simultaneous application of the six 397- and 866-nm laser tones necessary for Doppler cooling naturally leads to the formation of dark resonances at various laser frequency combinations. To simplify initial observation of ^{40}Ca^{+}, we start by trapping in a rf Paul trap configuration with a magnetic field of a few gauss to reduce the number of Doppler-cooling

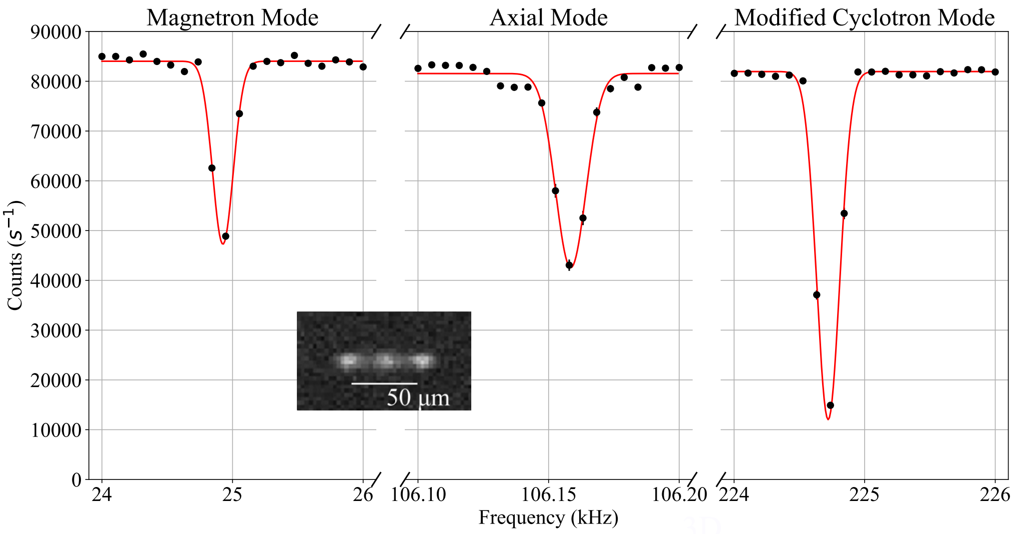

FIG. 4. Measurement of Penning trap secular frequencies obtained from the ion fluorescence response to a weak rf drive applied to a compensation electrode. The raw data (black points with error bars) and Gaussian fits (red curves) yield the three mode frequencies (magnetron, axial, and modified cyclotron). For many data points, the standard error is smaller than the point. Inset: Side-view image of the <10-ion planar array used for these measurements.

lasers and dark resonances as in Ref. [33], but here we use a series of permanent magnets of varying size and strength instead of electromagnet coils. We begin with only ≈3-G bias obtained from a 25-mm-diameter NdFeB ring magnet placed outside the vacuum chamber. The confining rf pseudopotential is generated by applying a 2.71-MHz sinusoidal rf drive to both endcap electrodes with a peak-to-peak rf amplitude of 500 V. Once initial trapping is observed and cooling is optimized at low magnetic field, we increase the field by moving the permanent magnet closer to the trap region until the ion fluorescence substantially decreases. We then reoptimize the Doppler laser cooling frequencies to maximize ion fluorescence. After hitting the maximal field for these smaller magnets, they are replaced with larger diameter and larger length magnets to continually raise the field until we reach the final magnet configuration. At several points in this procedure, we stop to tune the 423-nm laser to a field *sensitive* transition and record the resonant laser frequency of neutral ^{40}Ca as measured by the wavemeter. By recording the resonant frequency of the neutral Ca fluorescence and the corresponding optimized 397- and 866-nm laser cooling frequencies, we produce a look-up table for future reference that avoids deleterious dark resonances induced by the six laser cooling tones. By characterizing the field this way, we can repeatably return to the reference points in this process by finding the magnet placement that gives maximal neutral Ca fluorescence at the recorded field-sensitive 423-nm laser frequency. Once we reach the intended Penning trap field, we turn off the rf and load the Penning trap directly using an offset radial beam position to supply the proper torque to keep the cloud trapped [35].

To confine $^{40}\mathrm{Ca}^+$ in a harmonic axial potential, we apply -4 V to the segmented ring, $+1.47$ V to the compensation electrodes, and 0 V to the endcaps, where 0 V refers to the common vacuum chamber ground. We have performed ion trajectory simulations based on a finite element model of the trap electric field, and predict a trap axial frequency of 107.9 kHz. All trap electrodes are low-pass filtered at 60 Hz. We control the collective rotation rate, and hence the aspect ratio, of the ion array by adjusting either the common radial Doppler lasers' focal position or the individual 397- and 866-nm cooling frequencies. As shown in the bottom row of Fig. 1(c), we observe concentric circular shells in the cross-sectional fluorescence of two-dimensional (2D) arrays as in Ref. [36]. To estimate the radial ion temperature without modifying the applied optical torque, we apply a frequency-stabilized 729-nm laser beam that is resonant with the $|S_{1/2}, m_J = -1/2\rangle \rightarrow |D_{5/2}, m_J = -5/2\rangle$ electric quadrupole transition in $^{40}\mathrm{Ca}^+$. We tune the 729-nm laser frequency with an AOM and measure the $D_{5/2}$ state shelving probability versus quadrupole laser detuning. For 2D arrays with up to 20 ions, we measure a Gaussian full width at half maximum of 17.0(8) MHz, corresponding to a radial Doppler temperature upper bound of 133(13) mK. We note that this is a conservative bound on radial temperature, because the measured linewidth includes sidebands from the collective ion rotation (limited to 50 kHz for the 2D arrays presented here).

In addition to the neutral ^{40}Ca magnetometry, we also measure the modified cyclotron, axial, and magnetron frequencies of trapped $^{40}\mathrm{Ca}^+$ to determine the trap magnetic field. One can estimate the trap magnetic field confining a small single-species plasma using the measured trap mode frequencies and the Brown-Gabrielse invariance theorem (BGIT) [37–39]. The BGIT gives the relationship of the free-space cyclotron frequency ($f_c = eB/2\pi m$) to the frequencies of the measurable motional modes as $f_c^2 = f_-^2 + f_+^2 + f_z^2$, where f_- is the magnetron frequency, f_+ is the modified cyclotron frequency, f_z is the axial frequency, e is the electron charge, B is the magnetic field, and m is the $^{40}\mathrm{Ca}^+$ mass.

We measure the mode frequencies as described in Ref. [40], wherein a weak rf voltage is applied to one of the compensation electrodes and Doppler fluorescence is monitored as the rf frequency is varied. Typical scans of this type are shown in Fig. 4. These scans were taken at the optimal magnet spacing of 30 mm with a trapped 2D ion plane of <10 ions as depicted in the inset image of Fig. 4. Gaussian fits to these scans give a magnetron frequency of 24.926(28) kHz, an axial frequency of 106.159(3) kHz, and a modified cyclotron frequency of 224.721(24) kHz. The measured axial frequency agrees with the trajectory simulation prediction to within 2%, indicating minimal stray electric-field gradients from trap insulators. The BGIT yields a free-space cyclotron frequency of 249.781(2) kHz or, equivalently, a magnetic field of 6500.27(6) G for the pure sample of $^{40}\mathrm{Ca}^+$. The mode frequency measurement was performed at the $z = 0$ position of Fig. 2(b). The two different magnetic-field measurements (neutral versus ion) at $z = 0$ were taken on different days, and their 2(1)-G discrepancy is consistent with our observed day-to-day magnet temperature fluctuations of ≈100 mK.

IV. CONCLUSION

In conclusion, we have demonstrated a reconfigurable compact Penning trap compatible with Doppler laser cooling of single ions and trapped ion arrays. Our compact ion trap has a wide range of potential cold-ion physics applications including atomic and molecular ion spectroscopy, quantum simulation, and portable timekeeping. Straightforward modifications of this trap could include SmCo or radially magnetized REPMs for improved field stability or higher uniform magnetic field, respectively. Future work will include introduction of axial laser cooling via installation of reentrant viewports and trapping of the lower-mass ion species $^{9}\mathrm{Be}^+$ toward development of a compact frequency reference. The short-term magnetic-field instability of this trap will also be characterized via electron-spin resonance techniques and compared with that of traditional Penning traps [25].

ACKNOWLEDGMENTS

The authors thank John J. Bollinger, Nicholas D. Guise, Kenton R. Brown, Christopher M. Seck, and Roger C. Brown for helpful discussions and comments on the paper. This work was funded by Office of Naval Research Grant No. N00014-17-1-2408.

APPENDIX: MATHEMATICAL DESCRIPTION OF THE PERMANENT MAGNET FIELD PROFILE

Here we describe in more detail the procedure for fitting the measured axial magnetic-field curvature within the rare-earth permanent magnet Penning trap. The primary purpose of this Appendix is to provide the theoretical basis of our magnetic-field characterization and, for completeness, we also examine the consequences of using magnets with different remanent magnetizations. We will assume identical geometries (radii and lengths) for the magnets, because factory dimensional tolerances of ≈25 μm will not dominate observed deviations from ideal behavior for cm-scale magnets.

Reference [29] provides an analytic multipole expansion of the magnetic potential created by cylindrical permanent magnets. As the derivation assumes a scalar instead of a vector magnetic potential, it is valid only in free space. The magnetic scalar potential (Φ_M) for an azimuthally symmetric magnet may be expressed in the near-field limit as

$$\Phi_M = B_r \sum_{l=1}^{\infty} C_l r^l P_l\left(\frac{z}{r}\right) \tag{A1}$$

where B_r is the remanent magnetization, l is the multipole order, C_l are the multipole coefficients for the given magnet geometry, $r = \sqrt{\rho^2 + z^2}$ is the position coordinate, and P_l is the Legendre polynomial of order l. Specializing to the case of axial potentials ($\rho = 0$), Eq. (A1) may be simplified to

$$\Phi_M = B_r \sum_{l=1}^{\infty} C_l z^l \tag{A2}$$

where we have used the identity $P_l(1) = 1$. The axial magnetic field at position z, $B_z(z)$, is then just

$$B_z(z) = \frac{\partial}{\partial z}\Phi_M = B_r \sum_{l=1}^{\infty} l C_l z^{l-1}. \tag{A3}$$

Reproducing from [29] the multipole coefficients for axially semi-infinite rings (extending from z_0 to ∞) with an inner (outer) radius of ρ_1 (ρ_2) and *axial* magnetization, we have

$$C_l(\rho_1, \rho_2, z_0) = \begin{cases} \left.\frac{1}{2}\frac{z_0}{\sqrt{z_0^2+\rho^2}}\right|_{\rho_1}^{\rho_2}, & l = 1 \\ \left.\frac{1}{2l(l-1)}\frac{\rho P_{l-1}^1\left(z_0/\sqrt{\rho^2+z_0^2}\right)}{(\rho^2+z_0^2)^{l/2}}\right|_{\rho_1}^{\rho_2}, & l > 1 \end{cases}. \tag{A4}$$

To represent a magnet of finite length, L, spanning $[z_0, z_0 + L]$ with an overall magnetization in the $+z$ direction, we define

$$\widetilde{C}_l(\rho_1, \rho_2, z_0, L) \equiv C_l(\rho_1, \rho_2, z_0) - C_l(\rho_1, \rho_2, z_0 + L). \tag{A5}$$

1. Identical magnetizations, fit function

Following Eq. (A5), the total magnetic field, $B_z^{\mathrm{tot}}(z)$, due to a pair of identical magnets spaced apart by a vertical gap, g, and an overall offset of Δz from the origin is

$$B_z^{\mathrm{tot}}(z) = B_r \sum_{l=1}^{\infty} [\widetilde{C}_l(\rho_1, \rho_2, g/2, L) + \widetilde{C}_l(\rho_1, \rho_2, -g/2, L)] \times l(z - \Delta z)^{(l-1)}. \tag{A6}$$

The symmetry of the individual multipole coefficients $[C_l(\rho_1, \rho_2, -z_0) = (-1)^l C_l(\rho_1, \rho_2, z_0)]$ for axially magnetized rings [29] allows us to further simplify $B_z^{\mathrm{tot}}(z)$ as

$$B_z^{\mathrm{tot}}(z) = B_r \sum_{l=1}^{\infty} [1 - (-1)^l] \widetilde{C}_l(\rho_1, \rho_2, g/2, L) l(z - \Delta z)^{(l-1)}. \tag{A7}$$

Note that only odd-order multipoles (even-order magnetic-field curvatures) are nonzero for identical ring magnets in Eq. (A7). Equation (A7) is used to fit the measured magnetic-field profiles given in Fig. 2 of the paper by varying Δz, g, and B_r. As is pointed out in [29], there exists an "optimal" spacing, g_{opt}, where the multipole coefficient $\widetilde{C}_3(\rho_1, \rho_2, z_0, L)$ from each magnet is zero at the center of the magnet gap and the leading magnetic-field curvature is quartic instead of quadratic. This optimal spacing depends only on the magnet dimensions (ρ_1, ρ_2, L) and is computed numerically from Eq. (A5) in order to design a uniform-field Penning trap. We note that solid magnet cylinders $(\rho_1 = 0)$ also produce points of vanishing $\widetilde{C}_3(0, \rho_2, z_0, L)$, but designs making use of solid cylinders do not allow axial optical access and generally have smaller $g_{\rm opt}$ values for the same B_z at trap center.

2. Different magnetizations

We now estimate the effect of a mismatch between the top and bottom ring magnetizations caused by, for example, a temperature difference. We will define the following average $(\bar{B}_r)$ and differential (ΔB_r) magnetizations as

$$\begin{aligned} \bar{B}_r &\equiv \tfrac{1}{2}\big(B_r^{(t)} + B_r^{(b)}\big), \\ \Delta B_r &\equiv \tfrac{1}{2}\big(B_r^{(t)} - B_r^{(b)}\big), \end{aligned} \tag{A8}$$

where $B_r^{(t)}(B_r^{(b)})$ refers to the top (bottom) magnet remanence. To simplify notation from this point onward, we will also assume without loss of generality that $\Delta z = 0$. With these modifications, Eq. (A6) becomes

$$\begin{aligned} B_z^{\rm tot}(z) = {}& \bar{B}_r \sum_{l=1}^{\infty}[1-(-1)^l]\widetilde{C}_l(\rho_1, \rho_2, g/2, L) l z^{(l-1)} \\ &+ \Delta B_r \sum_{l=1}^{\infty}[1+(-1)^l]\widetilde{C}_l(\rho_1, \rho_2, g/2, L) l z^{(l-1)}. \end{aligned} \tag{A9}$$

We now compute the axial magnetic-field curvature (kth derivative) at the trap center due to each multipole order, distinguishing between even and odd multipoles:

$$\left.\frac{\partial^k B_z^{\rm tot}(z)}{\partial z^k}\right|_{z=0} = \begin{cases} 2\bar{B}_r(k+1)!\widetilde{C}_{k+1}(\rho_1, \rho_2, g/2, L), & k \text{ even} \\ 2\Delta B_r(k+1)!\widetilde{C}_{k+1}(\rho_1, \rho_2, g/2, L), & k \text{ odd} \end{cases}. \tag{A10}$$

Equation (A10) provides two key insights for Penning trap design with REPMs: (1) the optimal magnet gap for minimizing quadratic $(k = 2)$ curvature is independent of the relative magnetizations and (2) an imbalance in magnet remanence contributes odd-order field curvature at the trap center that is otherwise absent by symmetry.

---

[1] M. P. Bradley, J. V. Porto, S. Rainville, J. K. Thompson, and D. E. Pritchard, Phys. Rev. Lett. **83**, 4510 (1999).

[2] D. Hanneke, S. Fogwell, and G. Gabrielse, Phys. Rev. Lett. **100**, 120801 (2008).

[3] S. Sturm, A. Wagner, B. Schabinger, J. Zatorski, Z. Harman, W. Quint, G. Werth, C. H. Keitel, and K. Blaum, Phys. Rev. Lett. **107**, 023002 (2011).

[4] C. Smorra, S. Sellner, M. J. Borchert, J. A. Harrington, T. Higuchi, H. Nagahama, T. Tanaka, A. Mooser, G. Schneider, M. Bohman, K. Blaum, Y. Matsuda, C. Ospelkaus, W. Quint, J. Walz, Y. Yamazaki, and S. Ulmer, Nature (London) **550**, 371 (2017).

[5] D. J. Wineland, R. E. Drullinger, and F. L. Walls, Phys. Rev. Lett. **40**, 1639 (1978).

[6] J. J. Bollinger, D. J. Heinzen, W. M. Itano, S. L. Gilbert, and D. J. Wineland, IEEE Trans. Instrum. Meas. **40**, 126 (1991).

[7] N. Shiga, W. M. Itano, and J. J. Bollinger, Phys. Rev. A **84**, 012510 (2011).

[8] J. F. Goodwin, G. Stutter, R. C. Thompson, and D. M. Segal, Phys. Rev. Lett. **116**, 143002 (2016).

[9] G. Stutter, P. Hrmo, V. Jarlaud, M. K. Joshi, J. F. Goodwin, and R. C. Thompson, J. Mod. Opt. **65**, 549 (2018).

[10] E. Jordan, K. A. Gilmore, A. Shankar, A. Safavi-Naini, J. G. Bohnet, M. J. Holland, and J. J. Bollinger, Phys. Rev. Lett. **122**, 053603 (2019).

[11] M. A. van Eijkelenborg, M. E. M. Storkey, D. M. Segal, and R. C. Thompson, Phys. Rev. A **60**, 3903 (1999).

[12] B. M. Jelenković, A. S. Newbury, J. J. Bollinger, W. M. Itano, and T. B. Mitchell, Phys. Rev. A **67**, 063406 (2003).

[13] J. G. Bohnet, B. C. Sawyer, J. W. Britton, M. L. Wall, A. M. Rey, M. Foss-Feig, and J. J. Bollinger, Science **352**, 1297 (2016).

[14] J. W. Britton, B. C. Sawyer, A. C. Keith, C.-C. J. Wang, J. K. Freericks, H. Uys, M. J. Biercuk, and J. J. Bollinger, Nature (London) **484**, 489 (2012).

[15] M. Gärttner, J. G. Bohnet, A. Safavi-Naini, M. L. Wall, J. J. Bollinger, and A. M. Rey, Nat. Phys. **13**, 781 (2017).

[16] M. J. Biercuk, H. Uys, J. W. Britton, A. P. VanDevender, and J. J. Bollinger, Nat. Nanotech **5**, 646 (2010).

[17] K. A. Gilmore, J. G. Bohnet, B. C. Sawyer, J. W. Britton, and J. J. Bollinger, Phys. Rev. Lett. **118**, 263602 (2017).

[18] J. Lemaire, S. Thomas, A. Lopes, E. Louarn, H. Mestdagh, H. Latappy, J. Leprovost, and M. Heninger, Sensors **18**, 1415 (2018).

[19] V. Gomer, H. Strauss, and D. Meschede, Appl. Phys. B **60**, 89 (1995).

[20] L. Suess, C. D. Finch, R. Parthasarathy, S. B. Hill, and F. B. Dunning, Rev. Sci. Instrum. **73**, 2861 (2002).

[21] J. N. Tan, S. M. Brewer, and N. D. Guise, Rev. Sci. Instrum. **83**, 023103 (2012).

[22] S. M. Brewer, J. M. Dreiling, N. D. Guise, S. F. Hoogerheide, A. S. Naing, and J. N. Tan, Phys. Rev. A **98**, 032501 (2018).

[23] Y. Kawai, K. Shimizu, A. Noguchi, S. Urabe, and U. Tanaka, J. Phys. B **50**, 025501 (2017).

[24] T. Ruster, C. T. Schmiegelow, H. Kaufmann, C. Warschburger, F. Schmidt-Kaler, and U. G. Poschinger, Appl. Phys. B **122**, 254 (2016).

[25] J. W. Britton, J. G. Bohnet, B. C. Sawyer, H. Uys, M. J. Biercuk, and J. J. Bollinger, Phys. Rev. A **93**, 062511 (2016).

[26] D. J. Heinzen, J. J. Bollinger, F. L. Moore, W. M. Itano, and D. J. Wineland, Phys. Rev. Lett. **66**, 2080 (1991).

[27] H. F. Powell, S. R. d. Echaniz, E. S. Phillips, D. M. Segal, and R. C. Thompson, J. Phys. B **36**, 961 (2003).

[28] T. Hasegawa, M. J. Jensen, and J. J. Bollinger, Phys. Rev. A **71**, 023406 (2005).

[29] V. Frerichs, W. G. Kaenders, and D. Meschede, Appl. Phys. A **55**, 242 (1992).

[30] M. J. Biercuk, H. Uys, A. P. Vandevender, N. Shiga, W. M. Itano, and J. J. Bollinger, Quantum Info. Comput. **9**, 920 (2009).

[31] The wavemeter-based laser frequency servo consists of a software proportional-integral feedback loop that corrects the ECDL tuning piezoelectric voltage. The frequency error signal is created from a ≈1-ms-duration wavelength measurement obtained via serial communication with a Fizeau wavemeter that is stabilized to the atomic absorption of a cesium line at 852 nm.

[32] D. M. Lucas, A. Ramos, J. P. Home, M. J. McDonnell, S. Nakayama, J.-P. Stacey, S. C. Webster, D. N. Stacey, and A. M. Steane, Phys. Rev. A **69**, 012711 (2004).

[33] K. Koo, J. Sudbery, D. M. Segal, and R. C. Thompson, Phys. Rev. A **69**, 043402 (2004).

[34] D. R. Crick, S. Donnellan, D. M. Segal, and R. C. Thompson, Phys. Rev. A **81**, 052503 (2010).

[35] W. M. Itano, L. R. Brewer, D. J. Larson, and D. J. Wineland, Phys. Rev. A **38**, 5698 (1988).

[36] S. L. Gilbert, J. J. Bollinger, and D. J. Wineland, Phys. Rev. Lett. **60**, 2022 (1988).

[37] L. S. Brown and G. Gabrielse, Phys. Rev. A **25**, 2423 (1982).

[38] R. S. Van Dyck, F. L. Moore, D. L. Farnham, and P. B. Schwinberg, Phys. Rev. A **40**, 6308 (1989).

[39] J. V. Porto, Phys. Rev. A **64**, 023403 (2001).

[40] D. J. Wineland, J. J. Bollinger, and W. M. Itano, Phys. Rev. Lett. **50**, 628 (1983).